ADVANCED ENERGY MATERIALS
www.advenergymat.de

Electrocatalytic Ammonia Oxidation to Nitrite and Nitrate with NiOOH-Ni

Hanwen Liu, Cheng-Jie Yang, Chung-Li Dong, Jiashu Wang, Xin Zhang, Andrey Lyalin, Tetsuya Taketsugu, Zhiqi Chen, Daqin Guan, Xiaomin Xu, Zongping Shao, and Zhenguo Huang**

Ammonia electrooxidation in aqueous solutions can be a highly energy-efficient process in producing nitrate and nitrite while generating hydrogen under ambient conditions. However, the kinetics of this reaction are slow and the role of catalyst in facilitating ammonia electrooxidation is not well understood. In this study, a high-performance NiOOH-Ni catalyst is introduced for converting ammonia into nitrite with Faraday efficiency of up to 90.4% and nitrate production rate of 1 mg h^{-1} cm^{-2}. By employing *Operando* techniques, the role of NiOOH catalyst is elucidated in the dynamic electrooxidation of ammonia. Density functional theory (DFT) calculations support experimental observations and reveal the mechanism of the electrochemical oxidation of ammonia to nitrite and nitrate. Overall, this research contributes to the development of a cost-effective and highly efficient catalyst for large-scale ammonia electrolysis, while shedding light on the underlying mechanism of the NiOOH catalyst in ammonia electrooxidation.

1. Introduction

Ammonia electrooxidation plays a crucial role in environmental remediation and energy storage within the realm of catalytic reactions.[1] On one hand, ammonia electrooxidation can convert ammonia into nitrite and nitrate in wastewater to reduce the toxicity.[2] But this can have environmental and public health implications when nitrite and nitrate are not properly managed or controlled. To address this, biological treatment such as anammox process, and chemical treatment such as ion exchange can remove nitrite and nitrate.[3] At the same time, nitrate and nitrite are critical chemicals in modern society and their syntheses typically rely on Ostwald process that is energy intensive and generates pollutants. Therefore, electrooxidation of ammonia to produce nitrite and nitrate has attracted strong research interest since this process can take place at room temperature with low energy consumption and much-enhanced safety.[4]

Ammonia electrooxidation can be coupled with hydrogen production which can potentially improve the economic value of the process and maximize environmental benefit.[2b,5] To overcome this challenge, researchers have studied a series of catalysts such as Pt, Ir,[6] $[IrO_2]_x$ nanoclusters, and $[Cu(bipyalk)]^+$.[7] However, the use of these catalysts is subject to various limitations such as high

H. Liu, J. Wang, X. Zhang, Z. Huang
School of Civil and Environmental Engineering
University of Technology Sydney
Sydney, NSW 2007, Australia
E-mail: zhenguo.huang@uts.edu.au

H. Liu, D. Guan, X. Xu, Z. Shao
WA School of Mines: Minerals
Energy and Chemical Engineering (WASM-MECE)
Curtin University
Perth, WA 6102, Australia

C.-J. Yang, C.-L. Dong
Department of Physics
Tamkang University
Tamsui 25137, Taiwan

The ORCID identification number(s) for the author(s) of this article can be found under https://doi.org/10.1002/aenm.202401675

DOI: 10.1002/aenm.202401675

A. Lyalin, T. Taketsugu
Department of Chemistry
Faculty of Science
Hokkaido University
Sapporo 060-0810, Japan
E-mail: lyalin@icredd.hokudai.ac.jp

A. Lyalin
Research Center for Energy and Environmental Materials (GREEN)
National Institute for Materials Science
Namiki 1-1, Tsukuba 305-0044, Japan

T. Taketsugu
Institute for Chemical Reaction Design and Discovery (WPI-ICReDD)
Hokkaido University
Sapporo 001-0021, Japan

Z. Chen
ARC Centre of Excellence for Electromaterials Science
Intelligent Polymer Research Institute
AIIM Facility
Innovation Campus
University of Wollongong
Wollongong, NSW 2500, Australia

costs.[8] Nickel (Ni) and other transition metals such as cobalt and iron, have been extensively used as electrocatalysts owing to their abundance and remarkable catalytic activity.[9] Recent research has demonstrated that Ni facilitated the conversion of ammonia into nitrogen through electrooxidation,[10] and at higher potentials nitrite and nitrate can be obtained.[11] Besides, studies have shown that nickel hydroxide ($Ni(OH)_2$) and nickel oxyhydroxide (NiOOH) also possess catalytic capabilities for the ammonia electrooxidation.[12] $Ni(OH)_2$ transforms into NiOOH when reaching a certain working potential.[13] However, current references have limited understanding of the mechanism of how the NiOOH catalysts facilitate ammonia electrooxidation.

In this study, we employed a facile electrooxidation approach to synthesize NiOOH on Ni foam (NiOOH-Ni) as the catalyst for ammonia electrooxidation. NiOOH provides active sites that facilitate the conversion of ammonia into nitrite and nitrate, while Ni foam enhances conductivity and reaction kinetics. The NiOOH-Ni catalyst significantly improved the yield of nitrite (achieving a Faraday efficiency of 90.4%) and nitrate (1 mg h^{-1} cm^{-2}). We also employed *Operando* techniques and density functional theory (DFT) calculations to elucidate the reaction mechanisms of how NiOOH catalyzed ammonia electrooxidation. Specifically, *Operando* X-ray absorption near edge structure (XANES) revealed that NiOOH-Ni had a faster increase in the valence state than Ni foam when the working potential was increased. *Operando* X-ray absorption fine structure (XAFS) analysis confirmed the formation of the active NiOOH layer on the Ni foam catalyst. Time-of-flight secondary ion mass spectrometry (TOF-SIMS) revealed the dispersion and depth profiles of O^{2-}, OH^- and NO_3^- ions on NiOOH-Ni, demonstrating the dominant role of NiOOH in catalyzing ammonia electrooxidation. This study reports a cost-effective yet highly efficient NiOOH-Ni catalyst for ammonia electrooxidation. It also reveals the catalytic mechanisms of NiOOH on ammonia electrooxidation.

2. Results and Discussion

The NiOOH-Ni was synthesized via facile electrooxidation of Ni foam (**Figure 1a**). Typically, Ni foam was electrooxidized in 0.2 M NH_3+0.1 M K_2SO_4 electrolyte for 12 h to generate NiOOH-Ni (Figure S1, Supporting Information). The Ni foam exhibits relatively smooth surface (Figure S2, Supporting Information), and after the reaction, particles appear on the surface (Figure S3, Supporting Information). Transmission electron microscopy (TEM) and energy dispersive X-ray (EDX) mapping reveal that these particles are amorphous and consist of Ni and O (Figure S4, Supporting Information). The experimental identification of the NiOOH phase in the catalyst is shown in Raman spectra, which reveals two peaks at 481 and 560 cm^{-1} corresponding to the E_g and A_{1g} phonon modes in the NiOOH-based materials (Figure S5a, Supporting Information).[14] X-ray photoelectron spectroscopy (XPS) results reveal a strong presence of Ni^{2+} and Ni^{3+} in the NiOOH-Ni catalyst (Figure S5b,c, Supporting Information) which corresponds to β-NiOOH.[15]

The electrocatalytic performance of NiOOH-Ni and Ni catalysts was assessed by cyclic voltammetry (CV). The onset potential of NiOOH-Ni is 1.2 V_{RHE}, while the onset potential of Ni catalyst is 1.4 V_{RHE}, indicating the NiOOH-Ni is more active (Figure 1b). As potential increased, the current density of NiOOH-Ni is much higher than that of Ni catalyst, suggesting the NiOOH-Ni is more efficient than Ni catalyst.[13] The current density is mainly contributed from ammonia oxidation reaction (AOR), Ni oxidation, and oxygen evolution reaction (OER).[16] Further investigation using the I-T test revealed that NiOOH-Ni and Ni catalysts exhibited stable current densities of 25 and 6 mA cm^{-2}, respectively, in a 0.2 M NH_3 + 0.1 M KOH electrolyte (Figure S6, Supporting Information).

In the initial stages of oxidation, ammonia and hydroxyl ions undergo adsorption on the catalyst's surface. To assess the binding capacity, a Laviron analysis was performed using CV scanning at varying rates (Figures S7 and S8, Supporting Information). The redox peak current exhibited a linear relationship with the square root of the scanning rate, suggesting that the redox reaction is diffusion-controlled.[17] According to the Laviron equation, the redox constants (K_s) for NiOOH-Ni and Ni catalysts were determined to be 0.13 and 0.05 s^{-1}, respectively (Figure 1c). A higher value of the constant indicates that the NiOOH-Ni has a stronger affinity for ammonia and hydroxyl groups.[18] In the absence of ammonia in a 0.1 M KOH electrolyte, both NiOOH-Ni and Ni catalysts demonstrated relatively lower K_s values of 0.08 s^{-1} and 0.01 s^{-1}, respectively (Figures S9 and S10, Supporting Information). The contrasting K_s values in the two electrolytes highlight the catalyst's capacity to bind with both hydroxyl ions and ammonia.

To assess the intrinsic activity of the catalysts toward ammonia electrooxidation, linear sweep voltammetry (LSV) of NiOOH-Ni and Ni was performed in 0.2 M NH_3 + 0.1 M KOH electrolyte and 0.1 M KOH electrolyte, respectively (Figure 1d). Without NH_3, an onset potential of 1.1 V_{RHE} associated with the oxidation of Ni was observed for NiOOH-Ni.[19] In comparison, the onset potential of Ni was 1.35 V_{RHE} in 0.1 M KOH. With the addition of NH_3, the AOR increased the current density. For NiOOH-Ni, the onset potential was still ≈1.1 V_{RHE}, while it was ≈1.2 V_{RHE} for the Ni catalyst. To evaluate the reaction kinetics of AOR, we first extracted the AOR contribution by deducting current densities associated with Ni oxidation and OER. As in Figure 1d, the current density in shaded area is associated with AOR and was used to calculate the Tafel slope (inset).[20] The corresponding Tafel slope of NiOOH-Ni (139 mV dec^{-1}) is much smaller than that of Ni (667 mV dec^{-1}), suggesting that NiOOH-Ni possesses faster reaction kinetics toward AOR.[21] Furthermore, electrochemical active surface area (ECSA) tests revealed that NiOOH-Ni exhibits a higher active area compared to Ni (Figures S11 and S12, Supporting Information).[22] The LSV curves normalized by ECSA show that the intrinsic activity of NiOOH-Ni is higher than Ni (Figure S13, Supporting Information). However, electrochemical impedance spectroscopy (EIS) results demonstrated that the Ni catalyst possesses superior conductivity to NiOOH-Ni (Figure S14, Supporting Information).[9d] Overall, the catalytic performance of NiOOH-Ni can be attributed to the energetically favorable adsorption of ammonia allowing its deprotonation at the relatively small potentials, rapid reaction kinetics for AOR, and a high surface area with electrochemical activity. Additionally, the performance of NiOOH-Ni was also compared to that of pure NiOOH catalyst (Figure S15, Supporting Information). Pure NiOOH exhibited higher resistance than NiOOH-Ni, indicating that the presence of Ni foam effectively enhances the conductivity of NiOOH-Ni. Furthermore, pure NiOOH displayed a higher

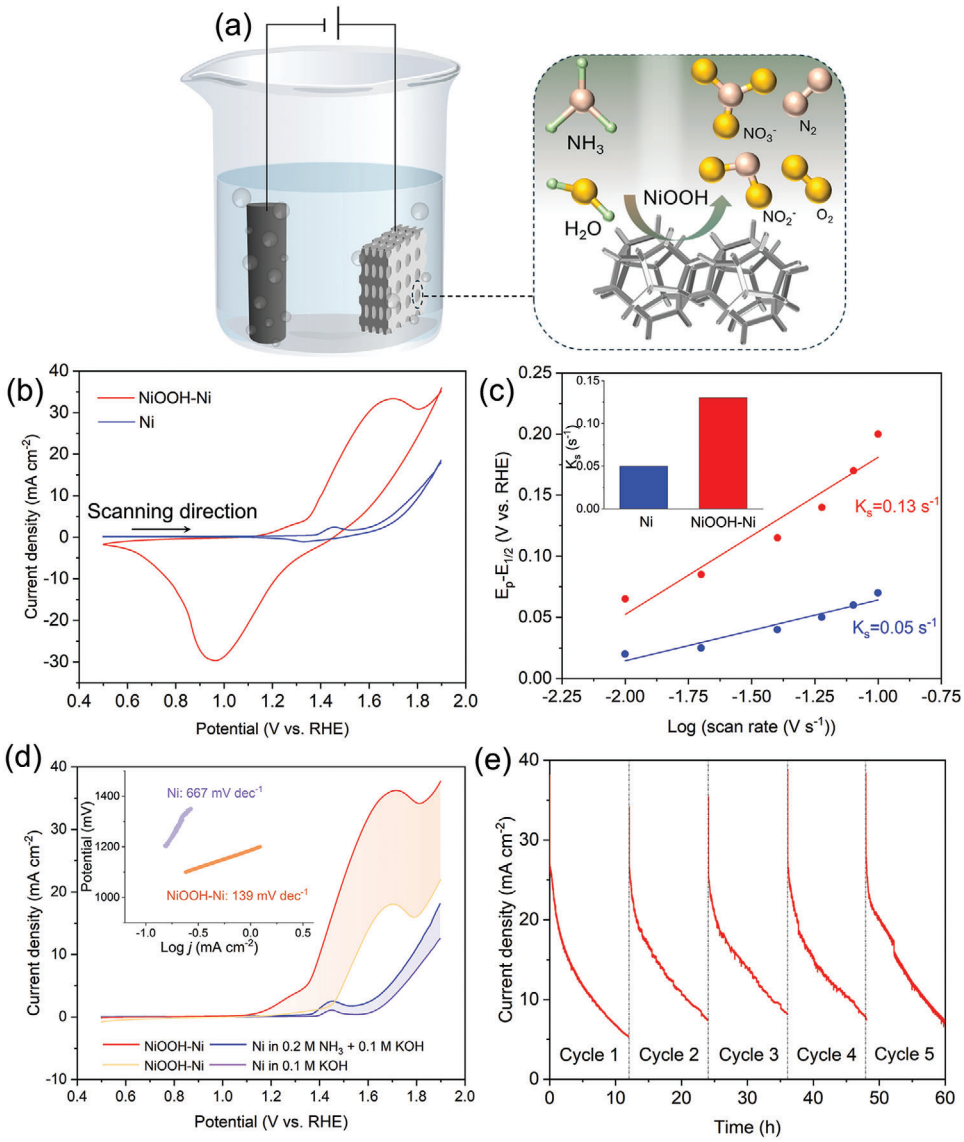

Figure 1. a) Schematic illustration of NiOOH-Ni preparation and its electrocatalytic function. b) CV curves at the first cycle. c) Redox peak potentials versus the logarithm of scan rates. Inset: Corresponding K_s. d) LSV curves of NiOOH-Ni and Ni in 0.2 M NH_3 + 0.1 M KOH electrolyte and 0.1 M KOH electrolyte, respectively, and the Tafel slopes (inset) associated with AOR of NiOOH-Ni and Ni in shaded area. e) Cycling stability of the NiOOH-Ni catalyst.

onset potential. However, both NiOOH and NiOOH-Ni demonstrated similar current densities in the I-T test (≈25 mA cm^{-2}) at 1.9 V_{RHE}, suggesting that the primary catalytic site is NiOOH not Ni. The role of Ni foam is to provide support for NiOOH particles and improve conductivity and reaction kinetics.

To test the cycling stability, the NiOOH-Ni electrode underwent five I-T tests (Figure 1e), with each cycle lasting 12 h. As the reaction progressed, ammonia was continuously consumed, leading to a decrease in current density. In the subsequent cycle, new electrolyte was used, and the current density recovered. This result demonstrates the stable catalysis of NiOOH-Ni for AOR (Figure S16, Supporting Information). Compared with Pt and Cu which have shown catalytic activity for AOR,[23] NiOOH-Ni demonstrates much higher current densities (Figure S17, Supporting Information). Furthermore, we observed that both the current density and conductivity increased with more concentrated ammonia (Figure S18, Supporting Information). Similarly, when the alkaline concentration was elevated, the current density of NiOOH-Ni also increased (Figure S19, Supporting Information). This effect can be attributed to the increased number of hydroxyl ions and ammonia, leading to a reduction in impedance and facilitating faster reaction kinetics (Figure S20, Supporting Information).

After evaluating the electrocatalytic performance, we studied the catalytic product at various working potentials. At 1.4 V_{RHE}, we observed the generation of nitrite (NO_2^-) under the catalysis of NiOOH-Ni (**Figure 2a**). The yield of nitrite was determined to be 0.16 ± 0.01 mg h^{-1} cm^{-2}. As the potential increased to 1.5

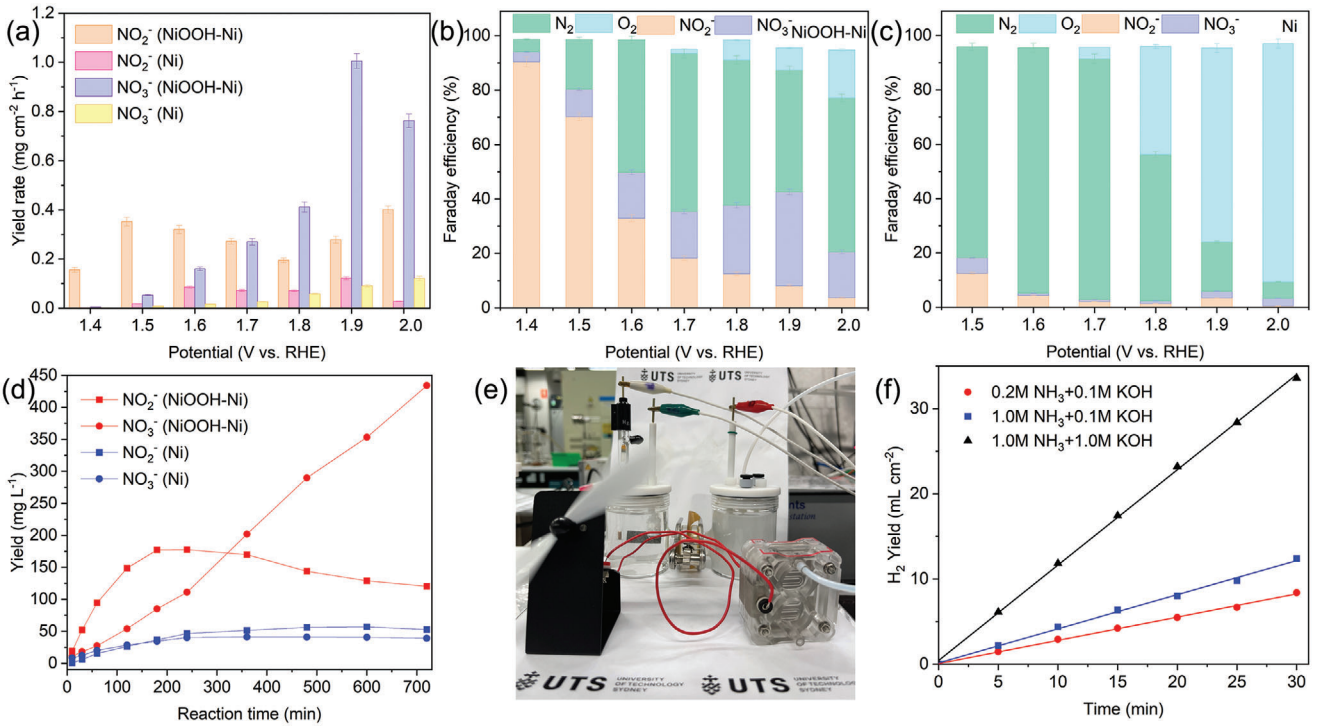

Figure 2. Yield of the ammonia electrolysis. a) Yield of nitrite and nitrate in 0.2 M NH_3 and 0.1 M KOH electrolyte for 12 h. b) Faraday efficiency of products from NiOOH-Ni catalyst. c) Faraday efficiency of products from Ni catalyst. d) Yield of nitrite and nitrate along with reaction time at 1.9 V_{RHE}. e) Digital image of the reaction cell for simultaneous H_2 production and AOR. f) Yield of hydrogen gas from NiOOH-Ni catalyst.

V_{RHE}, the NO_2^- yield reached a peak of 0.35 ± 0.02 mg h^{-1} cm^{-2}. However, further increasing the potential gradually resulted in the reduction of the nitrite yield, reaching its lowest value of 0.19 ± 0.01 mg h^{-1} cm^{-2} at 1.8 V_{RHE}. Subsequently, the yield increased again, reaching a maximum of 0.4 ± 0.02 mg h^{-1} cm^{-2} at 2.0 V_{RHE}. Meanwhile, the nitrate yield consistently increased with the working potential, peaking at 1.0 ± 0.03 mg h^{-1} cm^{-2} at 1.9 V_{RHE}. Thereafter, the nitrate yield slightly decreased to 0.76 ± 0.03 mg h^{-1} cm^{-2} at 2.0 V_{RHE}. In comparison, the Ni catalyst exhibited significantly lower nitrite and nitrate yields, in agreement with its low current density (Figure S21, Supporting Information).

The production of NO_2^- using the NiOOH-Ni catalyst exhibits the highest Faraday efficiency of 90.4 ± 1.8% at 1.4 V_{RHE} (Figure 2b). At a slightly higher potential of 1.5 V_{RHE}, NO_2^- production increased but the Faraday efficiency dropped to 70.2 ± 1.8% due to the rise of nitrate (NO_3^-). As the working potential further increased, the corresponding current density also increased, however, the Faraday efficiency of NO_2^- gradually decreased. Conversely, the efficiency of NO_3^- continued to increase and reached a maximum of 34.6 ± 1.1% at 1.9 V_{RHE}. As the potential was over 1.7 V_{RHE}, OER competed with AOR resulting in the production of oxygen gas. This phenomenon is more prominent under the impact of Ni catalyst (Figure 2c). The NiOOH-Ni catalyst is more NO_2^- selective compared to Ni catalyst when the potential is below 1.8 V_{RHE} because the Ni^{3+} in NiOOH can promote the oxidation of ammonia to nitrite through intermediate stages like $*NH_2$ and *NOH (discussed in following DFT calculation). The presence of oxyhydroxide species in NiOOH facilitates a catalytic pathway that favors the formation of NO_2^-. This pathway involves the stepwise oxidation of ammonia through various intermediates that are stabilized by the NiOOH surface. Meanwhile, the Ni catalyst is selective for N_2 due to the absence of oxyhydroxide species, and there is less stabilization of partial oxidation intermediates, leading to a higher selectivity for N_2.

Given that NO_3^- had its highest production at 1.9 V_{RHE}, we further examined the variation of NO_2^- and NO_3^- with respect to reaction time at that potential (Figure 2d). The NO_3^- concentration consistently increased along with the oxidation of ammonia. After a 12-hour reaction, the yield of NO_3^- reached 434 mg L^{-1} for NiOOH-Ni, whereas it is only 39 mg L^{-1} for Ni catalyst. Concerning NO_2^-, its yield initially surged within the first 3 h of reaction in the case of NiOOH-Ni. Subsequently, a portion of NO_2^- underwent further oxidation, resulting in an increase in NO_3^- yield. The highest yield of NO_2^- is 177 mg L^{-1} for NiOOH-Ni, compared to 56 mg L^{-1} for Ni. To further prove the oxidation effect of NiOOH-Ni on nitrite, NiOOH-Ni catalyst was used to oxidize nitrite in 0.1 M KNO_2 + 0.1 M KOH electrolyte. After 12 h reaction, most of nitrite was oxidized with the production of 3175 mg L^{-1} nitrate (Figure S22, Supporting Information). Overall, the NiOOH-Ni catalyst demonstrates superior catalytic performance over Ni to produce NO_2^- and NO_3^-. The highest Faraday efficiency of NO_2^- (90.4 ± 1.8%) was achieved at 1.4 V_{RHE}. Meanwhile, the highest Faraday efficiency of NO_3^- (34.6 ± 1.1%) was achieved at 1.9 V_{RHE} for NiOOH-Ni. Herein, we compared literature catalysts with NiOOH-Ni in terms of Faraday efficiency and yield, and NiOOH-Ni has the advantage of high catalytic yield (Table S1, Supporting Information).[4,7,12]

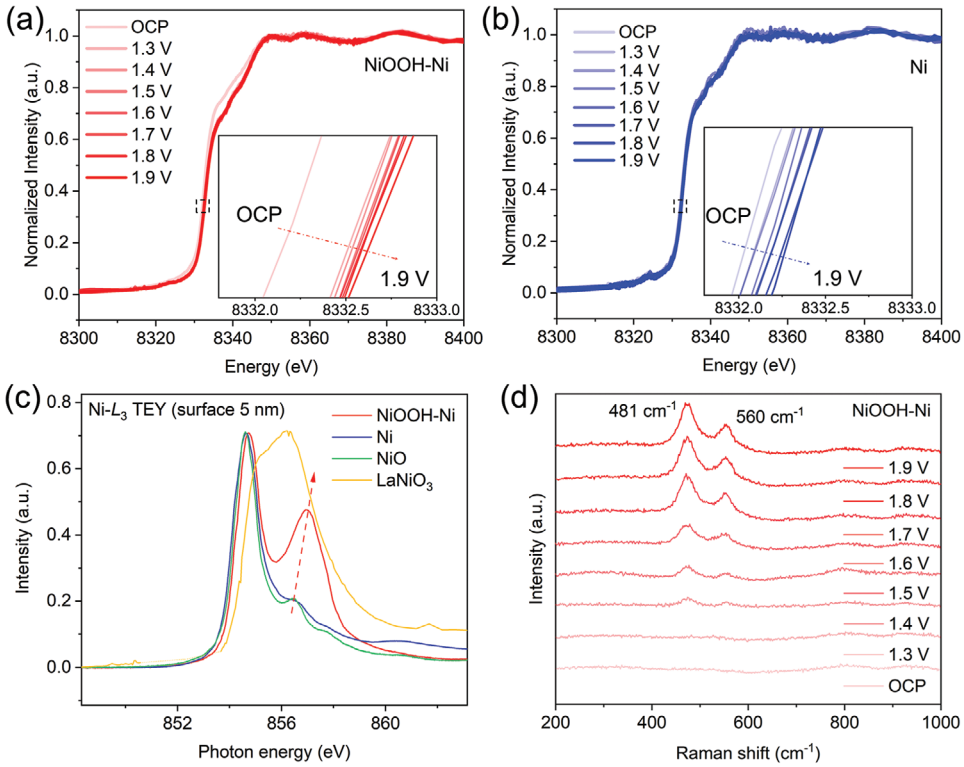

Figure 3. Chemical change of catalyst during electrocatalysis. *Operando* Ni K-edge XANES of a) NiOOH-Ni and b) Ni foam. The insets show zoom-in view of the edge shifts at different potentials in the area marked by dashed boxes. c) Ni-L_3 XAS spectra in TEY mode for NiOOH-Ni, Ni foam, NiO, and $LaNiO_3$. d) Raman spectra of NiOOH-Ni at different potentials.

Furthermore, we developed a device for simultaneous HER and AOR utilizing a NiOOH-Ni anode and a Ni_2P-Ni cathode (Figure S23, Supporting Information). An anion exchange membrane was used to separate the anodic and cathodic electrolytes while enabling OH^- exchange between the two chambers (Figure 2e). Specifically, the anodic electrolyte consisted of a mixture of ammonia and alkaline solution, while the cathodic electrolyte contained only alkaline solution. The membrane prevents ammonia from entering the cathodic cell and poisoning the hydrogen fuel cell. The generated hydrogen was subsequently directed into a hydrogen fuel cell, which effectively converted the hydrogen into electricity and powered a small fan with ease. The fuel cell exhibited an output voltage and current of 1.77 V and 52.5 mA, respectively (Figure S24, Supporting Information). We examined the influence of ammonia concentration and alkali concentration on the yield of hydrogen (Figure 2f). Within 30 min, the hydrogen yield reached 8.4 mL cm^{-2} when employing an electrolyte with 0.2 M NH_3+0.1 M KOH. It is worth noting that the pH of the electrolyte decreased slightly from 13.1 to 13.0 during this process (Figure S25, Supporting Information). Furthermore, an increase in ammonia concentration to 1.0 M led to a hydrogen yield of 12.4 mL cm^{-2}. Notably, in the 1.0 M NH_3+1.0 M KOH electrolyte, the hydrogen yield rose significantly to 33.6 mL cm^{-2}. This outcome highlights the significant impact of alkaline concentration on hydrogen production, as a higher OH^- concentration enhances conductivity and reduces the energy barrier associated with hydrogen evolution.[24]

To reveal the mechanism of AOR, *Operando* Ni K-edge XANES was employed to analyze the change in Ni valence state on NiOOH-Ni and Ni catalysts during the electrocatalytic reaction (**Figure 3**a,b). In 0.2 M NH_3+0.1 M electrolyte, the Ni valence state of NiOOH-Ni anode increased with the increase of working potential.[19] Compared to the Ni foam catalyst, the oxidation process in NiOOH-Ni occurs at a significantly faster rate. Specifically, the position of the Ni K-edge of NiOOH-Ni at 1.3 V is energetically higher than that in Ni foam at 1.9 V, meaning that the Ni valence in NiOOH-Ni at 1.3 V is already higher than that of Ni foam at 1.9 V. Considering that the onset potential of NiOOH-Ni for AOR is much lower than that of the Ni catalyst, it can be inferred that the electrocatalytic activity of NiOOH-Ni originates from the high-valence Ni species.[25] As the potential continues to increase, the increase in valence becomes less pronounced, indicating that the surface of NiOOH-Ni has been fully oxidized.

To verify the Ni valence states, soft X-ray absorption spectroscopy (XAS) was used to analyze NiOOH-Ni, Ni foam, NiO, and $LaNiO_3$. NiO and $LaNiO_3$ are reference materials representing Ni^{2+} and Ni^{3+}, respectively. The material surface valence states were examined through Ni L_3-edge XAS in the surface-sensitive total electron yield (TEY) mode. The center of the L_3-edge peak demonstrated a discernible shift to higher energy, indicating the augmentation of the 3d metal valence state (Figure 3c). By comparing their photon energy and intensity in the soft XAS spectra, it can be concluded that the surface Ni valence state of Ni foam after AOR was of Ni^{2+}. The appearance of the high energy peak at ≈856.4 eV in XAS of NiOOH-Ni demonstrates increased

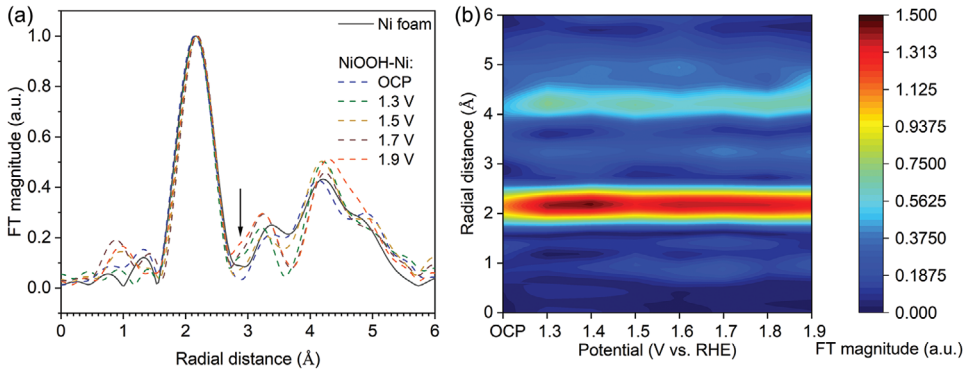

Figure 4. In situ identification of chemical bonds during electrocatalysis. The phase uncorrected Fourie transformed k^2 weighted *Operando* XAFS of NiOOH-Ni. a) FT magnitude normalized by the main peak. b) Operando XAFS of NiOOH-Ni in 2D plan. Vertical arrow indicates contribution from the first Ni-Ni coordination shell in NiOOH.

contribution from Ni^{3+}. Considering the significant catalytic differences between NiOOH-Ni and Ni in AOR, it is reasonable to say that Ni^{3+} is the main active site for the AOR on NiOOH-Ni electrode.

The potential-dependent formation of catalytically active sites is an interesting question that requires further investigation. Here, we used quasi-in situ Raman spectroscopy to follow the changes. The spectrum collected at the open circuit potential (OCP) revealed broad and weak peaks ≈800 and 950 cm^{-1}, corresponding to the Ni-O bond on the surface of NiOOH-Ni (Figure 3d). This observation suggests that a small amount of NiO is present on the surface of NiOOH-Ni in the OCP state. In contrast, the broad Ni-O band only appeared as the potential increased to 1.3 V_{RHE} for the Ni foam (Figure S26, Supporting Information). At 1.4 V_{RHE}, two peaks appeared at 481 and 560 cm^{-1}, indicating the presence of NiOOH.[26] These peaks intensify as the potential increased because the oxidizing potential drove the formation of Ni^{3+}. In contrast, these two peaks were invisible in the case of the Ni sample at any voltage. Given the superior catalytic performance of NiOOH-Ni compared to the Ni catalyst, it can be inferred that NiOOH is the active species for AOR.

To investigate how NiOOH facilitates AOR, *Operando* X-ray absorption fine structure (XAFS) was employed to monitor the in situ changes in chemical bonds during electrocatalysis (**Figure 4**). As a reference, the black line in Figure 4a demonstrates XAFS of a pure Ni foam sample in the air. A prominent sharp peak in the radial distribution of the phase uncorrected Fourie transform (FT) of the k^2 weighted fine-structure function χ(k) at 2.2 Å corresponds to the nearest Ni-Ni coordination in the Ni metal bulk (the Ni-Ni bond distance is 2.49 Å), while the less intensive broad peaks at ≈3.4, 4.2 Å, with a shoulder at 4.7 Å correspond to the superposition of the second, third and fourth coordination shells in metal Ni (Ni-Ni distances 3.52, 4.3, and 4.97 Å), respectively. At OCP the *Operando* XAFS of NiOOH-Ni (blue dashed line in Figure 4a) is very similar to that of a pure Ni, as the main signal comes from the Ni metal substrate. However, already at 1.3 V a wide shoulder at ≈2.8 Å appears from the left side of the second Ni-Ni coordination peak of a pure Ni. This shoulder is due to the contribution of the first shell Ni-Ni coordination (the Ni-Ni distance is 2.95 Å) and the second shell of Ni-O coordination (Ni-O distances ≈3.5 Å) in NiOOH structure.[14b] Therefore, one can suggest that the appearance of this shoulder can indicate the presence of a growing thin layer of NiOOH on the Ni foam. The intensity of this shoulder increases with the increase in the applied potential up to 1.9 V_{RHE}, except for the narrow interval of 1.5–1.6 V. This is due to the ammonia electrooxidation which disturbs the ordered structure of the thin NiOOH layer. It has been reported that pure Ni has a scarce activity to N compared to other catalysts such as Pt.[27] Consequently, the high-valence Ni^{3+} species in NiOOH-Ni facilitate and promote the adsorption of ammonia and related intermediates.

To understand the distribution of oxygen and nitrogen on the NiOOH-Ni electrocatalyst, we employed TOF-SIMS. The focused ion beam (FIB) maps can reveal the spatial element distribution. The selected area of NiOOH-Ni (Figure S27, Supporting Information) is covered by oxygen, except for some cracks where Ni foam is exposed (**Figure 5**a). In the depth profile, the oxygen content is decreasing with the majority of oxygen being on the top of NiOOH-Ni (Figure 5b). In contrast, the surface of Ni foam has only sparse oxygen coverage (Figures S28 and S29, Supporting Information). After running 72 h for AOR in 0.2 M NH_3 + 0.1 M KOH electrolyte at 1.9 V, the Ni foam electrode was only partially oxidized (Figure S30, Supporting Information). A small amount of NO_3^- was detected on the top of the surface, overlapping with the O^{2-} dispersion.

In the case of NiOOH-Ni, OH^- overlaps with O^{2-} on the top surface (Figure S31, Supporting Information). Nitrate distribution spreads from the surface to the interior of the structure (Figure S32, Supporting Information), indicating the nitrogen has good affinity with NiOOH. The concentration of nitrate decreased from the top surface along the depth profile (Figure S33, Supporting Information). In Figure 5c, the nitrate distribution is highly overlapping with oxygen and hydroxide. It should be noted that the intensity of nitrate is low at the cracks, indicating the heterostructure between NiOOH and Ni is not the main active site for AOR. Thermogravimetric analysis (TGA) confirms that the ratio of NiOOH in NiOOH-Ni is 13 wt.% (Figure S34, Supporting Information).

To get deeper insights into the mechanism of AOR by NiOOH, we have performed spin-polarized density functional theory (DFT) calculations to elucidate the possible reaction pathways. To describe adequately the catalyst structure, we have adopted

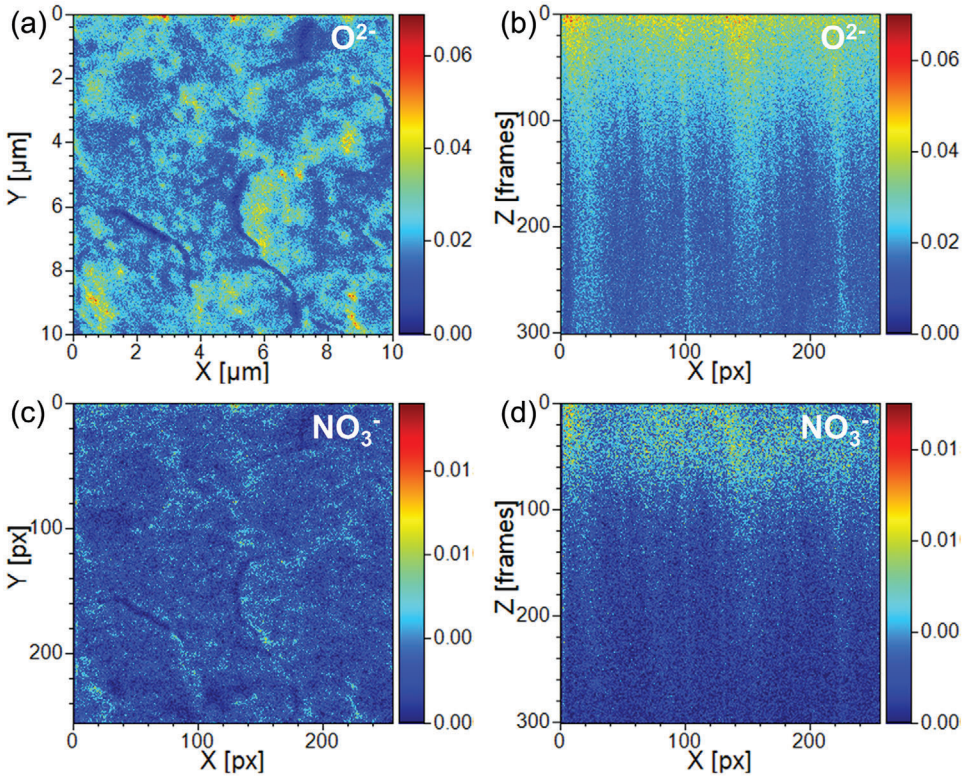

Figure 5. TOF-SIMS elemental maps of different elements from NiOOH-Ni. FIB map of a) O on the surface; b) O^{2-} depth profile; c) NO_3^- on the surface; d) NO_3^- depth profile.

the theoretical model for the bulk β-NiOOH proposed by Carter et al.[28] Comprehensive details regarding the theoretical and computational methods are provided in the supporting information. For the formation of nitrate, the AOR under alkaline conditions can be written in the following form:

$$NH_3\,(g) + 9OH^-\,(aq) \rightarrow NO_3^-\,(aq) + 6H_2O + 8e^- \quad (1)$$

where (g) and (aq) refer to the gas and aqueous phases, respectively.

To analyze energetics of the electrochemical process (1) we use the concept of computational hydrogen electrode (CHE) introduced by Nørskov et al.,[29] which allows us to express the electrochemical potentials of proton $\mu(H^+)$ and hydroxyl anion $\mu(OH^-)$ in a solution of the arbitrary pH at a given electrode potential (U_{SHE} or U_{RHE}).[30] Here U_{SHE} and U_{RHE} are the potentials on the standard and reversible hydrogen electrode scales, respectively. In this work, we will refer to the RHE scale as it is usually used in most experimental studies.

Despite the apparent simplicity of the reaction (1), it is a complicated multi-electron transfer process accompanied by the transfer of nine hydroxyl anions OH^- in alkaline media. The conventional mechanism of this electrochemical reaction consists of the following elementary steps:

$$NH_3 + * \rightarrow * NH_3 \quad (2)$$

$$* NH_3 + OH^- \rightarrow * NH_2 + H_2O + e^- \quad (3)$$

$$* NH_2 + OH^- \rightarrow * NH + H_2O + e^- \quad (4)$$

$$* NH + OH^- \rightarrow * N + H_2O + e^- \quad (5)$$

$$* N + OH^- \rightarrow * NOH + e^- \quad (6)$$

$$* NOH + OH^- \rightarrow * NO + H_2O + e^- \quad (7)$$

$$* NO + OH^- \rightarrow * NO_2H + e^- \quad (8)$$

$$* NO_2H + OH^- \rightarrow * NO_2 + H_2O + e^- \quad (9)$$

$$* NO_2 + OH^- \rightarrow * NO_2H + e^- \quad (10)$$

$$* NO_2H + OH^- \rightarrow NO_3^- + H_2O \quad (11)$$

Here the first step (2) is the adsorption of ammonia molecule on the catalytically active site, denoted by asterisk (*), next three steps (3)–(5) are related to the subsequent deprotonation of the adsorbed intermediates coupled with the electron transfer and formation of the water molecules. In the next step (6) the hydroxyl anion adsorbs on the reaction intermediate with the formation of the N-O bond, followed by the OH^- attack (7) with consequent deprotonation of this intermediate and formation of a water molecule. A similar process occurs in the pairs of (8, 9), and (10, 11), resulting in the release of the NO_3^- anion in the last step (11). We have also found an alternative pathway,

$$* NOH + OH^- \rightarrow * N(OH)_2 + e^- \quad (12)$$

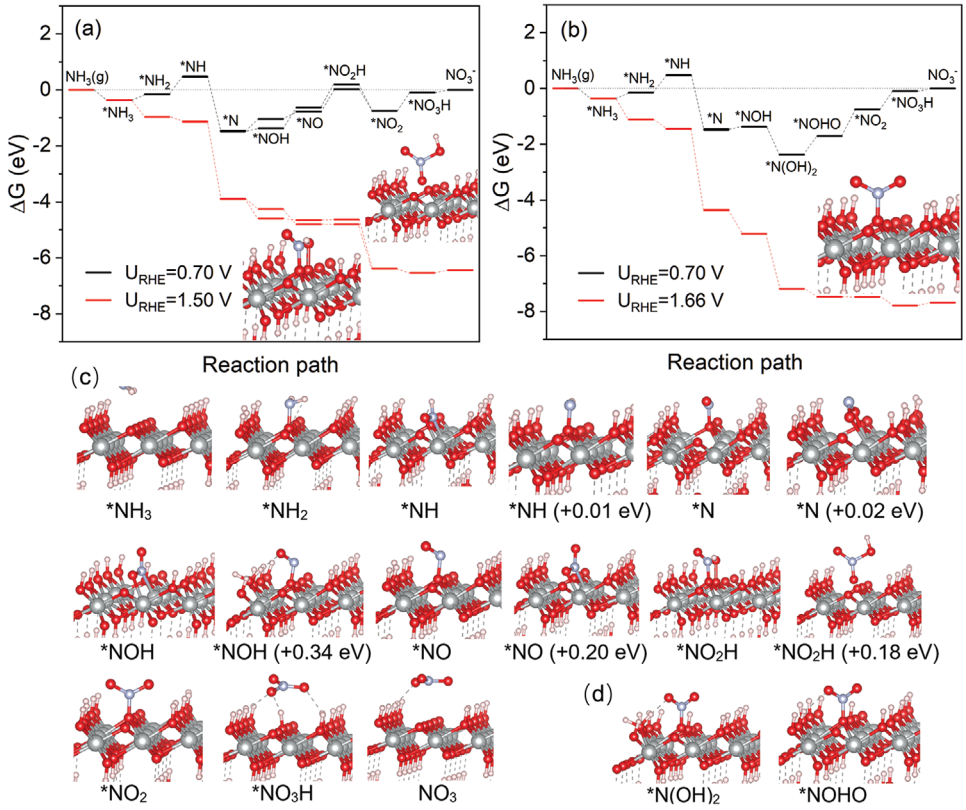

Figure 6. Free energy diagram for electrochemical oxidation of ammonia to nitrate along the a) conventional and b) alternative (via (12, 13) steps) reaction pathways calculated at the equilibrium potential (0.70 V_{RHE}) (black lines) and limiting potentials (red lines). The key intermediate structures for the reaction limiting steps are shown in insets. Ni, O, N, and H atoms are shown in grey, red, light grey, and light pink colors, respectively. The optimized structures of the intermediates for (c) conventional (2)–(11) pathway and d) intermediates leading to the alternative pathway via (12, 13) steps. The numbers in parathesis refer to the energy of the isomeric configuration with respect to the most stable structure of the corresponding intermediate.

$$* N(OH)_2 + OH^- \rightarrow * NO_2H + H_2O + e^- \quad (13)$$

where instead of *NOH deprotonation in (7), additional adsorption of OH^- occurs (12) followed by the deprotonation of the $*N(OH)_2$ species in (13).

The change in the Gibbs free energy ΔG_n for each elementary step n of the reaction (1) can be obtained using the free energies of the reaction intermediates $G(i) = E_{el}(i) + E_{ZPE}(i) - TS(i)$ and Equation S2 (Supporting Information) giving an electrochemical potential of the hydroxyl anion $\mu(OH^-)$ – electron pair $\mu(e^-)$. Here $E_{el}(i)$ corresponds to the electron energy of the intermediate (i) obtained from the DFT calculations, $E_{ZPE}(i)$ and S(i) are the zero-point energy and entropy of the intermediate (i), respectively, while T is temperature. The zero-point energies $E_{ZPE}(i)$ have been calculated by summation of the vibrational frequencies over the normal modes, while entropies of free species were taken from the NIST Chemistry Webbook.[31] A similar approach has been used in recent theoretical works of Chen, Klinkova, et al.,[12,32] who considered electrochemical ammonia oxidation on the β-$Ni(OH)_2$ model catalyst. Comprehensive details on the calculations of ΔG can be found in ref. [32]. The theoretical value of the equilibrium potential obtained from the calculated Gibbs free energy of the reaction (1) is 0.70 V_{RHE}, in very good agreement with the value of −0.132 $V_{SHE,\ pH=14}$ reported in ref. [32]. To get structures of all intermediates along the reaction pathway we first modeled the adsorption of the ammonia molecule by putting it in several non-equivalent positions and orientations on the β-NiOOH surface and performing structural optimization, followed by subsequent deprotonation or OH addition. In each new step, we considered not only the most stable structure obtained in the previous step but also a number of the energetically low-lying isomers, because the less stable structures can be more reactive.[33] A similar approach has been successfully used in our previous works on the investigation of various chemical processes on surfaces and atomic clusters.[33,34]

Figure 6a demonstrates the free energy diagram calculated for ammonia electrooxidation on the β-NiOOH (0001) surface along the (2)–(11) pathway. The optimized structures of the key intermediates are shown in Figure 6c,d. In the first step (2), NH_3 adsorbs on the β-NiOOH surface with an adsorption energy of −0.37 eV. The subsequent deprotonation of $*NH_3$ leads to the formation of $*NH_2$ and *NH intermediates, which are energetically unfavorable at the equilibrium potential. The $*NH_2$ adsorbs on the low coordinated surface O atom with the formation of the O-N bond, while for *NH we found two energetically degenerated isomeric configurations with a negligible energy difference of 0.01 eV. In the first configuration, N interacts with the surface Ni atom, pulling one of the low coordinated oxygens above the surface with the formation of the oxygen vacancy (O_v) and O-N

bond; while in the second isomeric configuration, *NH adsorbs on top of the surface O.

The third deprotonation step (5) is energetically favorable at the equilibrium potential and results in the formation of the stable *N intermediate. We also found two energetically degenerated structural configurations with an energy difference of 0.02 eV, where the stripped N atom pulls one or two O atoms from the NiOOH surface, forming one or two O_v surface vacancies, respectively. Thus, *N is very reactive, resulting in the considerable local structural reorganization of the surface in the vicinity of *N and the formation of the *(O_v – NO) and *($2O_v$ – NO_2) like structural configurations.

The next step of OH^- adsorption (6) leads to the formation of two isomeric configurations of the *NOH intermediate with an energy difference of 0.34 eV. The most stable configuration is formed as a result of OH^- trapping by one of the oxygen vacancies in the *($2O_v$ – NO_2) structure, while the less stable structure is obtained by OH^- trapping oxygen vacancy in *(O_v – NO) structure with the spontaneous proton transfer to the nearest hydroxyl group on the surface (Figure 6). Deprotonation of these *NOH intermediates leads to the formation of two isomeric configurations of *NO with an energy difference of 0.2 eV. Notably, the most stable *NO structure is obtained from the deprotonation of the less stable *NOH, while the less stable *NO isomer is obtained from the deprotonation of the most stable *NOH intermediate. This feature results in competition between these isomeric configurations as a function of the applied potential. The next step along the conventional pathway (8) is the adsorption of OH^- on *NO intermediates. This step leads to the formation of two isomers of *NO_2H intermediates with an energy difference of 0.18 eV. The most stable *NO_2H configuration is obtained as a result of OH^- adsorption next to the most stable *NO isomer. The energetically less stable isomer is obtained by direct OH^- attack of the less stable *NO configuration, with the formation of the NO_3H structure, trapped by O_v site, as shown in Figure 6. The deprotonation of both *NO_2H isomers results in the formation of the stable *NO_2 intermediate, followed by additional OH^- adsorption and deprotonation in (10), (11), and the final release of the (NO_3^-) product.

As one can see from Figure 6 (black lines), reaction (1) cannot proceed at the equilibrium potential, because of the numerous energetically unfavorable processes, where the free energy develops uphill. To drive the reaction, one should apply overpotential, making all reaction steps energetically favorable. We have found the limiting potential (the potential when the reaction can start) is U_{RHE} = 1.50 V, in excellent agreement with experimental observations (see, Figure 2a). Here the rate-limiting step is OH^- addition to *NO (step (8)) which is characterized by the largest positive change of the free energy ΔG(i) for this step. As already discussed, we have found two isomers for *NO and *NO_2H intermediates, which opens a competing reaction pathway with the limiting potential of U_{RHE} = 1.52 V.

We have also found that the adsorption of OH^- anion onto *NOH intermediate via step (12) is more energetically favorable than *NOH deprotonation (Figure 6b) and results in the formation of the formal *$N(OH)_2$ intermediate, shown in Figure 6b. This opens up an alternative reaction pathway (Figure 6b). In this case, the rate-limiting step is the deprotonation of the formal *NOHO intermediate at the limiting potential of U_{RHE} = 1.66 V. Thus, at the potentials above 1.66 V both reaction mechanisms shown in Figure 6a,b become possible, which should considerably favor the overall reaction, in accordance with experimental observations.

In the above analysis, we have considered the complete reaction of ammonia electrooxidation to nitrate (NO_3^-) which involves transfer of nine hydroxyl anions and eight electrons. However, ammonia electrooxidation can also lead to the formation of nitrite (NO_2^-) and/or molecular nitrogen (N_2) in the following reactions:

$$NH_3(g) + 7OH^-(aq) \rightarrow NO_2^-(aq) + 5H_2O + 6e^- \quad (14)$$

$$2NH_3(g) + 6OH^-(aq) \rightarrow N_2(g) + 6H_2O + 6e^- \quad (15)$$

Figure S35 (Supporting Information) demonstrates that the formation of NO_2^- product became possible at U_{RHE} = 1.50 V for the conventional, and U_{RHE} = 1.38 V for alternative pathways, respectively. Therefore, the formation of NO_2^- product can dominate in the interval of 1.38 V < U_{RHE} < 1.50 V, while the production of NO_3^- can start at U_{RHE} > 1.50 V and become dominant at U_{RHE} > 1.66 V, due to the opening of the additional pathway of NO_3^- production in full accordance with the experimental observations (Figure 2a).

On the other hand, the formation of N_2 gas can occur via the so-called Oswin and Salomon mechanism[35] as a result of dimerization of the N* species or Gerischer and Mauerer mechanism[36] as a result of possible dimerization of NH_2* and NH* species followed by their electrochemical oxidation to N_2. Our calculations demonstrate that N_2 formation can occur already at U_{RHE} = 1.33 V (see Figure S36, Supporting Information) from the thermodynamic point of view, where deprotonation of NH_2* to NH* is the potential determining step. Thus, the formation of the N_2 gas starts at a slightly lower potential than that for NO_2^- formation. However, at the low potentials, the N_2 formation on the NiOOH-Ni catalyst can be suppressed kinetically as a result of the high N-N coupling barrier, playing a role of the rate-determining step. With the increase in the potential, the height of such a barrier should decrease in accordance with the Brønsted–Evans–Polanyi (BEP) principle.[37] Therefore, N_2/NO_2^- product ratio can increase with the potential in full agreement with our experimental observations (Figure 2b).

3. Conclusion

In this study, we utilized a facile electrooxidation technique to synthesize NiOOH on Ni foam as a catalyst for ammonia electrooxidation. The low-cost NiOOH-Ni is highly efficient in catalyzing AOR and delivered a current density of 25 mA cm^{-2} in 0.2 M NH_3 + 0.1 M KOH and 150 mA cm^{-2} in 0.2 M NH_3 + 1.0 M KOH at 1.9 V_{RHE}, respectively. NiOOH-Ni catalyst led to a substantial enhancement in NO_2^- yield, achieving an impressive Faraday efficiency of 90.4% at 1.4 V_{RHE}, as well as NO_3^- production at a rate of 1 mg h^{-1} cm^{-2} at 1.9 V_{RHE}. Using NiOOH-Ni as the anodic catalyst, a prototype was set up for simultaneous green hydrogen production and ammonia oxidation. The prototype generated 8.4 and 33.6 mL cm^{-2} hydrogen gas from 0.2 M NH_3 + 1.0 M KOH electrolyte and 1.0 M NH_3 + 1.0 M KOH electrolyte in 30 min at 1.9 V_{RHE}, respectively. To gain insights

into the underlying reaction mechanism, *Operando* XANES analysis was employed, revealing a more rapid increase in the Ni oxidation state of NiOOH-Ni compared to Ni as the potential increased. Soft XAS demonstrated that the surface of Ni catalyst was composed of Ni^{2+}, while NiOOH-Ni was composed of Ni^{3+}. TOF-SIMS study revealed the dispersion of nitrate well below the surface of NiOOH-Ni, confirming the catalytic effect of NiOOH. Theoretical calculations revealed several competing reaction pathways for NH_3 electrocatalytic oxidation on the model β-NiOOH (0001) surface. The formation of NO_2^- product could dominate in the interval of $1.38\ V < U_{RHE} < 1.50\ V$ while the production of NO_3^- should dominate at $U_{RHE} > 1.66$ V, due to the opening of the alternative pathway in full accord with the experimental observations. This paper not only reports a cost-effective catalyst with exceptional efficiency for ammonia electrooxidation but also contributes to a deeper understanding of the catalytic mechanism of NiOOH-based catalysts.

4. Experimental Section

Materials: Nickel (Ni) foam was purchased from Xiamen Tmax Battery Equipments Limited. Potassium hydroxide (KOH), ammonia solution (37%), and potassium sulfate (K_2SO_4) were purchased from Sigma-Aldrich.

Synthesis: The NiOOH-Ni was synthesized via the following steps. First, Ni foam as the working electrode was immersed in 0.1 M NH_3+0.1 M K_2SO_4 electrolyte, together with HgO/Hg reference electrode and carbon rod counter electrode. The working potential was set to 2.0 V_{RHE}. After 12 h reaction, the NiOOH formed on the surface of Ni leading to NiOOH-Ni.

Materials Characterization: The morphology and micro-structure of the NiOOH-Ni and Ni foam were studied by scanning electron microscope (SEM), JSM-7500. XPS was conducted on a hemispherical energy analyzer (PHOIBOS 100/150). Operando XAS was carried out on TPS44A (Quick-scanning XAS, transmission mode) at the National Synchrotron Radiation Research Center (NSRRC, Taiwan), to obtain the surface and bulk chemical composition and structural information of materials. Soft XAS spectra at Ni-L_3 was conducted at the TLS BL20A of the NSRRC in Taiwan. FIB-ToF-SIMS was performed on an IONTOF V-100 instrument, Curtin University.

Electrochemical Measurements: Electrochemical experiments were performed in a typical three-electrode system connected to a CHI-760E (CHI Instruments). All potentials were referred to an SCE reference electrode, and carbon rod was used as the counter electrode in all measurements. All electrochemical data was presented without IR-correction. According to the equation: E (vs RHE) = E (vs SCE) + 0.0591*pH + 0.098, the potential was calibrated to the RHE. EIS tests were performed at different applied potentials versus RHE in the frequency range of 0.1–100 000 Hz.

Product Analysis: Nitrate and nitrite concentrations were determined by ion chromatography (IC) using Metrohm Eco IC equipped with an anion column using 3.2 mM Na_2CO_3 (>99.5%, Sigma) + 1 mM $NaHCO_3$ (>99.7% Sigma) solution in Milli-Q water as an eluent. The calibration curve standards, containing 1–10 ppm NO_3^-/NO_2^- were prepared from commercially available solutions of these anions (1000 ppm, Sigma). The samples for IC were prepared by 100-times dilution of the reaction mixture (100 uL of the reaction mixture was taken from the cell for each measurement). N_2 and O_2 concentrations were determined using an on-line gas chromatography (Agilent 8890) equipped with a thermal conductivity detector (TCD) at Curtin University. A home-made gas-tight H-type electrochemical cell was employed. The gaseous products formed during ammonia oxidation under certain potentials were directed to the GC for quantitative analysis. N_2 and O_2 was quantified based on an independent calibration using gases containing known concentrations of each gas.

Theoretical and Computational Methods: All calculations have been performed using the Perdue–Burke–Ernzerhof (PBE) exchange-correlation functional[38] with the Hubbard U corrections within the rotationally invariant Dudarev approach,[39] and the projector-augmented wave (PAW) method[40] as implemented in the Vienna ab initio Simulation Package (VASP).[41] Dispersion effects have been considered using the D3 Grimme's parametrization.[42] Recently, nickel oxyhydroxide-based catalysts attracted strong attention, mainly due to their remarkable electrocatalytic activity for water oxidation.[43] However, the detailed understanding of the catalytic processes on NiOOH surfaces is hindered by the structural complexity of this material, possessing different inter-transformable β-NiOOH and γ-NiOOH phases with a layered structure consistent with NiO_2 sheets.[43,44] The important difference between β-NiOOH and γ-NiOOH phases comes from the interlayer species, consisting of H atoms (protons), H_2O molecules, and metal atom cations in various structural arrangements, affecting the catalytic properties of NiOOH and giving rise to a mixture of Ni atoms in the different oxidation states, Ni^{2+}, Ni^{3+}, and Ni^{4+}.[28,43,45] In the present work, the most commonly used theoretical model for the bulk β-NiOOH proposed by Carter et al.,[28] was adopted with the lattice parameters of a = 2.947 Å, b = 5.984 Å, c = 5.004 Å, α = 89.41°, β = 70.34°, and γ = 120.56°. This model provides an adequate and accurate description of the β phase of the catalyst structure. The bulk structure has been used to construct the three NiO_2-layer (4 × 2) supercell for the most stable β-NiOOH (0001) surface. A vacuum layer of ≈17 Å was used to avoid interaction between the periodically replicated images. The topmost NiO_2 layer with H atoms was fully relaxed with an absolute force threshold of 0.01 eV $Å^{-1}$, while the bottom two layers were fixed. The Brillouin zone was sampled by the Γ-centered 2 × 2 × 1 k-point mesh.

To analyze energetics of the ammonia electrochemical oxidation, the concept of computational hydrogen electrode (CHE) introduced by Nørskov et al.,[27,29] is used which allows to express the electrochemical potential of the proton $\mu(H^+)$ in a solution of the arbitrary pH at a given electrode potential (see, e.g.,)[30] as:

$$\mu\left(H^+\right) + \mu\left(e^-\right) = 1/2\mu^0\left(H_2\right) - eU_{SHE} - k_BT\ln(10)\,pH = 1/2\mu^0\left(H_2\right) - eU_{RHE} \quad (16)$$

where $\mu(e^-)$ is the electrochemical potential of the electron, $\mu^0(H_2)$ is the chemical potential of hydrogen gas under standard conditions (T = 298.15 K, p_{H2} = 1 bar), k_B is a Boltzmann constant, T is a temperature, while U_{SHE} and U_{RHE} are the potentials on the standard and reversible hydrogen electrode scales, respectively. In this work, the RHE scale will be referred to as it is usually used in most experimental studies. In the case of an alkaline environment, it is more convenient to operate with the electrochemical potential of the solvated hydroxyl anion $\mu(OH^-)$, which can be expressed via $\mu(H^+)$ and the chemical potential of water $\mu^0(H_2O)$:[30b]

$$\mu\left(OH^-\right) = \mu^0\left(H_2O\right) - \mu\left(H^+\right) = \mu^0\left(H_2O\right) - 1/2\mu^0\left(H_2\right) + eU_{RHE} + \mu\left(e^-\right) \quad (17)$$

Supporting Information

Supporting Information is available from the Wiley Online Library or from the author.

Acknowledgements

Z.H. acknowledges support under the Australian Research Council's Discovery Projects funding scheme (project number DP220103458) and the Future Fellowship (FT190100658). This work was partly supported by the MEXT Program: Data Creation and Utilization-Type Material Research and Development Project Grant Number JPMXP1122712807. Calculations were performed using computational resources of the Institute for Solid State Physics, the University of Tokyo, Japan; and the Research Center for Computational Science, Okazaki, Japan (Project: 23-IMS-C016)

Open access publishing facilitated by University of Technology Sydney, as part of the Wiley - University of Technology Sydney agreement via the Council of Australian University Librarians.

Conflict of Interest

The authors declare no conflict of interest.

Data Availability Statement

The data that support the findings of this study are available from the corresponding author upon reasonable request.

Keywords

ammonia oxidation, AOR, HER, NiOOH, wastewater treatment

Received: April 12, 2024
Revised: July 16, 2024
Published online: August 7, 2024

[1] C. Zhong, W. Hu, Y. Cheng, *J. Mater. Chem. A.* **2013**, *1*, 3216.
[2] a) C. Zhang, D. He, J. Ma, T. D. Waite, *Water Res.* **2018**, *145*, 220; b) H. Liu, X. Xu, D. Guan, Z. Shao, *Energy Fuels.* **2024**, *38*, 919; c) L. Zhang, P. Jin, Z. Wu, B. Zhou, J. Jiang, A. Deng, Q. Li, T. Hussain, Y. Zhang, H. Liu, *Energy Environ. Mater.* **2024**, e12725.
[3] J. G. Kuenen, *Nat. Rev. Microbiol.* **2008**, *6*, 320.
[4] a) S. Cohen, S. Johnston, C. K. Nguyen, T. D. Nguyen, D. A. Hoogeveen, D. Van Zeil, S. Giddey, A. N. Simonov, D. R. MacFarlane, *Green Chem.* **2023**, *25*, 7157; b) X. Jiang, D. Ying, X. Liu, M. Liu, S. Zhou, C. Guo, G. Zhao, Y. Wang, J. Jia, *Electrochim. Acta.* **2020**, *345*, 136157; c) Y.-J. Shih, C.-H. Hsu, *Chem. Eng. J.* **2021**, *409*, 128024.
[5] a) Y. Li, H. Wang, C. Priest, S. Li, P. Xu, G. Wu, *Adv. Mater.* **2021**, *33*, 2000381; b) K. C. Ranjeesh, S. Kaur, A. K. Mohammed, S. Gaber, D. Gupta, K. Badawy, M. Aslam, N. Singh, T. Skorjanc, M. Finšgar, *Adv. Energy Mater.* **2024**, *14*, 2303068; c) K. Siddharth, Y. Hong, X. Qin, H. J. Lee, Y. T. Chan, S. Zhu, G. Chen, S.-I. Choi, M. Shao, *Appl. Catal. B.* **2020**, *269*, 118821.
[6] a) Y. T. Chan, K. Siddharth, M. Shao, *Nano Res.* **2020**, *13*, 1920; b) M.-H. Tsai, T.-C. Chen, Y. Juang, L.-C. Hua, C. Huang, *Electrochem. Commun.* **2020**, *121*, 106875; c) X. Wang, Q. Kong, Y. Han, Y. Tang, X. Wang, X. Huang, T. Lu, *J. Electroanal. Chem.* **2019**, *838*, 101.
[7] a) H.-Y. Liu, H. M. Lant, J. L. Troiano, G. Hu, B. Q. Mercado, R. H. Crabtree, G. W. Brudvig, *J. Am. Chem. Soc.* **2022**, *144*, 8449; b) H.-Y. Liu, H. M. Lant, C. C. Cody, J. Jelušic´, R. H. Crabtree, G. W. Brudvig, *ACS Catal.* **2023**, *13*, 4675; c) H.-Y. Liu, J. A. Jayworth, R. H. Crabtree, G. W. Brudvig, *ACS Catal.* **2024**, *14*, 2842.
[8] H. Kim, W. Yang, W. H. Lee, M. H. Han, J. Moon, C. Jeon, D. Kim, S. G. Ji, K. H. Chae, K.-S. Lee, *ACS Catal.* **2020**, *10*, 11674.
[9] a) H. Liu, K. Hu, D. Yan, R. Chen, Y. Zou, H. Liu, S. Wang, *Adv. Mater.* **2018**, *30*, 1800295; b) H. Liu, W.-H. Lai, H.-L. Yang, Y.-F. Zhu, Y.-J. Lei, L. Zhao, J. Peng, Y.-X. Wang, S.-L. Chou, H.-K. Liu, *Chem. Eng. J.* **2021**, *408*, 127348; c) H. Liu, W. Pei, W.-H. Lai, Z. Yan, H. Yang, Y. Lei, Y.-X. Wang, Q. Gu, S. Zhou, S. Chou, *ACS Nano.* **2020**, *14*, 7259; d) H. Liu, W.-H. Lai, Y. Liang, X. Liang, Z.-C. Yan, H.-L. Yang, Y.-J. Lei, P. Wei, S. Zhou, Q.-F. Gu, *J. Mater. Chem. A.* **2021**, *9*, 566; e) R. Wang, H. Liu, K. Zhang, G. Zhang, H. Lan, J. Qu, *Chem. Eng. J.* **2021**, *404*, 126795; f) M. Zhang, H. Li, X. Duan, P. Zou, G. Jeerh, B. Sun, S. Chen, J. Humphreys, M. Walker, K. Xie, *Adv. Sci.* **2021**, *8*, 2101299; g) F. Almomani, R. Bhosale, M. Khraisheh, A. Kumar, M. Tawalbeh, *Int. J. Hydrogen Energy.* **2020**, *45*, 10398; h) Z. Wu, Y. Liu, D. Wang, Y. Zhang, K. Gu, Z. He, L. Liu, H. Liu, J. Fan, C. Chen, *Adv. Mater.* **2024**, *36*, 2309470; i) P. Jin, L. Zhang, Z. Wu, B. Zhou, Z. Duan, H. Li, H. Liu, A. Deng, Q. Li, Y. Zhang, *Chem. Eng. J.* **2024**, *481*, 148303; j) X. S. Zhang, S. Mao, J. Wang, C. Onggowarsito, A. Feng, R. Han, H. Liu, G. Zhang, Z. Xu, L. Yang, *Nanoscale.* **2024**, *16*, 4628.
[10] M. Gonzalez-Reyna, M. S. Luna-Martínez, J. F. Perez-Robles, *Nanotechnology.* **2020**, *31*, 235706.
[11] S. Johnston, S. Cohen, C. K. Nguyen, K. N. Dinh, T. D. Nguyen, S. Giddey, C. Munnings, A. N. Simonov, D. R. MacFarlane, *ChemSusChem.* **2022**, *15*, 202200614.
[12] J. J. Medvedev, Y. Tobolovskaya, X. V. Medvedeva, S. W. Tatarchuk, F. Li, A. Klinkova, *Green Chem.* **2022**, *24*, 1578.
[13] Y.-J. Shih, Y.-H. Huang, C. Huang, *Electrochim. Acta.* **2018**, *263*, 261.
[14] a) B. S. Yeo, A. T. Bell, *J. Phys. Chem. C.* **2012**, *116*, 8394; b) D. Liu, Y. Yan, H. Li, D. Liu, Y. Yang, T. Li, Y. Du, S. Yan, T. Yu, W. Zhou, *Adv. Mater.* **2023**, *35*, 2203420; c) D. Chen, X. Xiong, B. Zhao, M. A. Mahmoud, M. A. El-Sayed, M. Liu, *Adv. Sci.* **2016**, *3*, 6.
[15] B. Wang, Q. Liu, Z. Qian, X. Zhang, J. Wang, Z. Li, H. Yan, Z. Gao, F. Zhao, L. Liu, *J. Power Sources.* **2014**, *246*, 747.
[16] J.-H. Kim, D. H. Youn, K. Kawashima, J. Lin, H. Lim, C. B. Mullins, *Appl. Catal. B.* **2018**, *225*, 1.
[17] Z. Xiao, Y.-C. Huang, C.-L. Dong, C. Xie, Z. Liu, S. Du, W. Chen, D. Yan, L. Tao, Z. Shu, *J. Am. Chem. Soc.* **2020**, *142*, 12087.
[18] J. Wang, L. Gan, W. Zhang, Y. Peng, H. Yu, Q. Yan, X. Xia, X. Wang, *Sci. Adv.* **2018**, *4*, eaap7970.
[19] J. Gallenberger, M. Li, H. M. Fernández, A. Alkemper, C. Tian, B. Kaisera, J. P. Hofmann, *Catal. Sci. Technol.* **2023**, *13*, 4693.
[20] V. Rosca, M. T. M. Koper, *Phys. Chem. Chem. Phys.* **2006**, *8*, 2513.
[21] F. J. Vidal-Iglesias, J. Solla-Gullón, V. Montiel, J. M. Feliu, A. Aldaz, *J. Phys. Chem. B.* **2005**, *109*, 12914.
[22] J. He, Y. Zou, Y. Huang, C. Li, Y. Liu, L. Zhou, C.-L. Dong, X. Lu, S. Wang, *Sci. Chin. Chem.* **2020**, *63*, 1684.
[23] A. M. Pourrahimi, R. L. Andersson, K. Tjus, V. Ström, A. Björk, R. T. Olsson, *Sustain. Energy Fuels.* **2019**, *3*, 2111.
[24] X. Wang, C. Xu, M. Jaroniec, Y. Zheng, S.-Z. Qiao, *Nat. Commun.* **2019**, *10*, 4876.
[25] J. J. Abed, S. Ahmadi, L. Laverdure, A. Abdellah, C. P. O'Brien, K. Cole, P. Sobrinho, D. Sinton, D. Higgins, N. J. Mosey, *Adv. Mater.* **2021**, *33*, 2103812.
[26] Y. Jin, S. Huang, X. Yue, H. Du, P. K. Shen, *ACS Catal.* **2018**, *8*, 2359.
[27] J. A. Herron, P. Ferrin, M. Mavrikakis, *J. Phys. Chem. C.* **2015**, *119*, 14692.
[28] J. M. P. Martirez, E. A. Carter, *Chem. Mater.* **2018**, *30*, 5205.
[29] a) J. K. Nørskov, J. Rossmeisl, A. Logadottir, L. Lindqvist, J. R. Kitchin, T. Bligaard, H. Jonsson, *J. Phys. Chem. B.* **2004**, *108*, 17886; b) A. A. Peterson, F. Abild-Pedersen, F. Studt, J. Rossmeisl, J. K. Nørskov, *Energy Environ. Sci.* **2010**, *3*, 1311.
[30] a) J. Huang, M. Li, M. J. Eslamibidgoli, M. Eikerling, A. Groß, *JACS Au.* **2021**, *1*, 1752; b) Q. Liang, G. Brocks, A. Bieberle-Hütter, *J. Phys. Energy.* **2021**, *3*, 026001.
[31] P. J. Linstrom, W. G. Mallard, *J. Chem. Eng. Data.* **2001**, *46*, 1059.
[32] R. M. Choueiri, S. W. Tatarchuk, A. Klinkova, L. D. Chen, *Electrochem. Sci. Adv.* **2022**, *2*, 2100142.
[33] M. Gao, A. Lyalin, S. Maeda, T. Taketsugu, *J. Chem. Theory Comput.* **2014**, *10*, 1623.
[34] a) H. C. Dinh, G. Elumalai, H. Noguchi, A. Lyalin, T. Taketsugu, K. Uosaki, *J. Chem. Phys.* **2023**, *158*, 134713; b) A. Lyalin, A. Nakayama, K. Uosaki, T. Taketsugu, *Phys. Chem. Chem. Phys.* **2013**, *15*, 2809.
[35] H. Oswin, M. Salomon, *Can. J. Chem.* **1963**, *41*, 1686.
[36] H. Gerischer, A. Mauerer, *J. Electroanal. Chem. Interfacial Electrochem.* **1970**, *25*, 421.
[37] a) J. Bronsted, *Chem. Rev.* **1928**, *5*, 231; b) M. Evans, M. Polanyi, *Trans. Faraday Soc.* **1938**, *34*, 11; c) A. Logadottir, T. H. Rod, J. K. Nørskov, B. Hammer, S. Dahl, C. Jacobsen, *J. Catal.* **2001**, *197*, 229.
[38] J. P. Perdew, K. Burke, M. Ernzerhof, *Phys. Rev. Lett.* **1996**, *77*, 3865.
[39] S. L. Dudarev, G. A. Botton, S. Y. Savrasov, C. Humphreys, A. P. Sutton, *Phys. Rev. B.* **1998**, *57*, 1505.

[40] P. E. Blöchl, *Phys. Rev. B.* **1994**, *50*, 17953.
[41] a) G. Kresse, J. Furthmüller, *Phys. Rev. B.* **1996**, *54*, 11169; b) G. Kresse, J. Furthmüller, *Comput. Mater. Sci.* **1996**, *6*, 15.
[42] S. Grimme, J. Antony, S. Ehrlich, H. Krieg, *J. Chem. Phys.* **2010**, *132*, 15.
[43] Y.-F. Li, J.-L. Li, Z.-P. Liu, *J. Phys. Chem. C.* **2021**, *125*, 27033.
[44] H. Bode, K. Dehmelt, J. Witte, *Electrochim. Acta.* **1966**, *11*, 1079.
[45] a) A. J. Tkalych, K. Yu, E. A. Carter, *J. Phys. Chem. C.* **2015**, *119*, 24315; b) A. Van der Ven, D. Morgan, Y. Meng, G. Ceder, *J. Electrochem. Soc.* **2005**, *153*, A210.